10TH INTERNATIONAL SYMPOSIUM ON PARTICLE IMAGE VELOCIMETRY - PIV13
Delft, The Netherlands, July 1-3, 2013

Application of Tomographic PIV in a Transonic Cascade

J. Klinner[1], C. Willert[1]

[1]Engine Measurement Techniques, Institute of Propulsion Technology,
German Aerospace Center (DLR), 51170 Köln, GERMANY
joachim.klinner@dlr.de

ABSTRACT

The contribution demonstrates the applicability of volumetric PIV in a highly loaded compressor cascade at $M_1 = 0.60$. Under these operation conditions the secondary flow structures in the cascade are dominated by a passage vortex located at the base of the blade and near the suction side. The application of volume resolving thick-sheet PIV (or tomo-PIV) near the trailing edge of the cascades blades is intended to demonstrate the techniques potential of instantaneously resolving secondary flow structures within the separation region of the cascade and its ability to derive three dimensional statistical data of fluctuations of velocity in the turbulent flow region. The report describes various aspects of the adaption of the tomographic PIV setup to the restricted access on the cascade wind tunnel. A four camera setup is was used to resolve a measuring volume of $36 \times 24 \times 4$ mm from which a total of $54 \times 74 \times 13$ vectors at a spacing of 0.64 mm in x (chord-wise direction) and a spacing of 0.32 mm in y and z could be recovered. The stability of the camera setup is documented by evaluating the image shifts of stationary features due to vibrations of the wind tunnel. Three dimensional reconstruction of the imaged particle volume is achieved with the maximum entropy reconstruction technique (MENT, [2, 6]) and validated against synthetic data as well as conventional MLOS-SMART reconstruction. The reconstruction quality of experimental data is documented by plots of the reconstructed intensity along volume depth. The extraction the three-dimensional displacement field relies on multi-resolution, 3-D correlation processing with iterative volume deformation. The recovered three-dimensional velocity fields are compared at selected planes with (thin-sheet) stereo PIV data.

1. INTRODUCTION

Tomographic PIV (tomo-PIV) and conventional stereo PIV (SPIV) are utilized in order to characterize the complex transonic flow within a highly loaded compressor cascade at $M_1 = 0.60$. In particular tomo-PIV has a high potential of recovering the three dimensional corner flow on the suction sides of the cascade blades. The oil-streak image shown in Fig. 1 taken from [3] provides an impression of the complex flow pattern at the intersection between end wall and the blades suction side. The flow is dominated by a passage vortex which is driven by the pitch-wise pressure gradient between pressure and suction side. The time-averaged location of the vortex is predicted by a RANS (Reynolds-averaged Navier Stokes) simulation as visualized in Fig. 2. The vortex and the reverse pressure gradient along the cascade passage cause a flow separation between the end wall and the blade. In particular the high shear between the main passage flow and the passage vortex induces strong velocity fluctuations in a compressor cascade which are responsible for the majority of total pressure losses in a compressor cascade. Furthermore the corner separation leads to blockage effects which limit the mass flow capacity of the cascade. Under the given test conditions the simulations predict an extension of the passage vortex region of approximately $40 \times 24 \times 15$ mm.

The application of volume resolving thick-sheet PIV (or tomo-PIV) near the trailing edge of the cascades blades is intended to demonstrate the techniques potential of instantaneously resolving secondary flow structures within the separation region of the cascade and its ability to derive three dimensional statistical data of fluctuations of velocity in the turbulent flow region.

2. Test facility and cascade geometry

The measurements are carried out in the transonic cascade wind tunnel (TGK) of the DLR Institute of Propulsion Technology. The TGK is a closed loop, continuously running facility with a half-symmetrical nozzle and a variable test section by adjustment of the lower end wall. Additional suction capacities of the system allow the control of the side wall boundary layer in front of the cascade test section, in the upper and lower bypass channels as well as the transonic upper end wall. The suction capacities allow the adjustment of the static pressure across the channel height. Thereby, a homogeneous inflow according to an ”infinite blade cascade” is achieved. The cascade consists of seven airfoils that are supported by transparent acrylic side walls of 16 mm thickness which provide suitable optical access for schlieren visualisation as well as flow velocity methods such as laser-2-focus velocimetry (L2F) and particle image velocimetry (PIV). Geometry parameters and operation conditions of the cascade are summarized in table 1.

3. Experimental Setup

Measurements are carried out near the suction side of a single passage in an area coincident with the numerically predicted location of the passage vortex. Fig. 3 shows a photograph of the tomographic PIV setup which involves four double-frame (PIV) cameras fitted with Scheimpflug mounts to account for the oblique imaging arrangement. The view parameters are summarized in table 2. Two

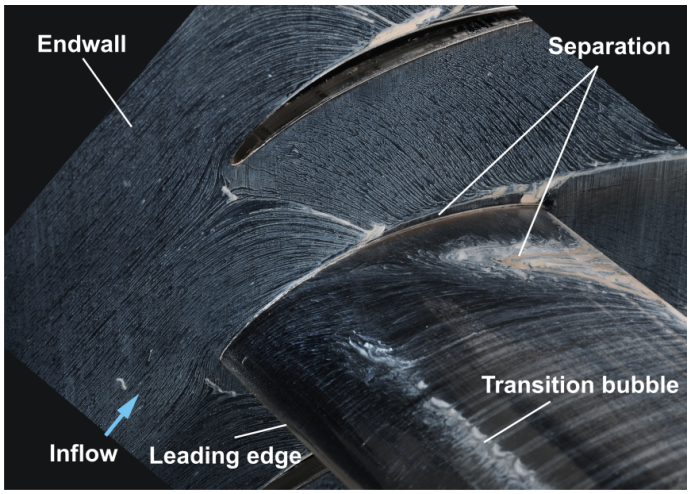

Figure 1: Oil streak pattern of surface shear [3]

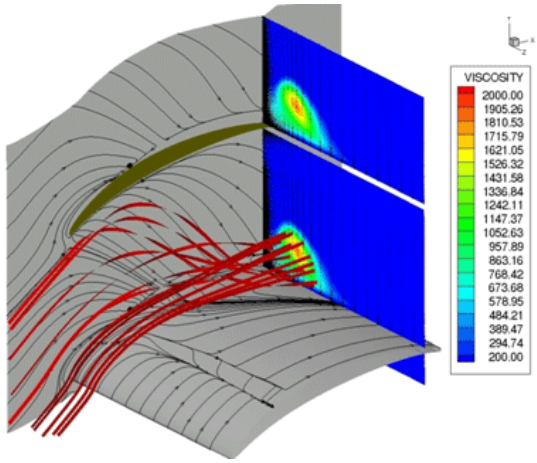

Figure 2: RANS Simulation, color represents eddy viskosity

Table 1: Cascade parameter

Chord length	70 mm
Pitch	40.4 mm
Span width	168 mm
Deflection angle	43°
M_1 at aerodynamic design point	0.60
Re based on chord length	800,000
Free stream turbulence Tu_1	$1-4\%$

cameras observe the volume of interest along the suction side at zero pitch while the other camera pair observes the measurement volume from above at 26°and 34°pitch in order to have a sufficient angular aperture of the system.

Both single-axis and two-axis Scheimpflug mounts are used to optimize the depth of focus of each camera. The f-numbers range from 8...16 in order to minimize optical distortions due to the oblique viewing through the Perspex window. The observed common region of interest has a size of approximately 36×24 mm and is located near the trailing edge of the blade. The thickness of the illuminated volume was successively adjusted to approximately 1 and 3.5 mm FWHM during each wind tunnel run. Volumetric image data was acquired in three regions at distances of 4, 8 and 11 mm with respect to the side wall in order to cover the entire corner vortex. Each region has a maximum size of $36 \times 24 \times 4$ mm^3 depending on the sheet thickness. Within each region three additional thin sheet stereo PIV measurements were recorded and later used for comparison.

Table 2: Imaging parameter of Tomographic Setup

		Camera 1	Camera 2	Camera 3	Camera 4
Region of interest	[pixel]	1600×1200	1600×1030	1900×1500	2048×1800
Approx. magnification M	[-]	0.37	0.31	0.38	0.46
Approx. magnification M	[px/mm]	50	42	51	62
Focal length	[mm]	100	100	85	100
f-number nominal / effective	[-]	16 / 22	11 / 14	8 / 11	11 / 16
Particle image density at thick sheet	[ppp]	0.018	0.024	0.022	0.015
Particle Image diameter	[px]	3...5	2...4	2...4	3...4
Yaw / pitch angle		30°/-26°	-15°/-34°	-15°/ 0°	26°/ 0°

The light sheet probe (see Fig. 5) is positioned 450 mm downstream of the trailing edge of the cascade. The beam enters the cascade through a 500 mm long, 16 mm diameter probe whose tip contains a 90° deflecting mirror. The length of the light sheet probe is required to allow access to the opposite side of the tunnel. The probe is additionally supported from the inside of the tunnel in order to reduce aerodynamically induced bending and vibrations which would affect the light sheet position. Previously conducted PIV measurement campaigns showed that the tunnel flow carries significant amounts of rust particles whose high momentum can lead to a fast erosion of the reflective coating on the 90° turning mirror at the light-sheet probe's tip. To improve the protection of the mirror surface from incoming particles (rust) the probe tip was retrofitted with a Laval nozzle which redirects and accelerates the purge flow against the tunnel flow, ideally at supersonic speed [4]. Thereby incoming particles are sufficiently decelerated and prevent the erosion of mirror surface.

As illustrated in Fig. 5 the optical setup of the probe contains two doublets at the probe entry, the first of which reduces the laser-beam

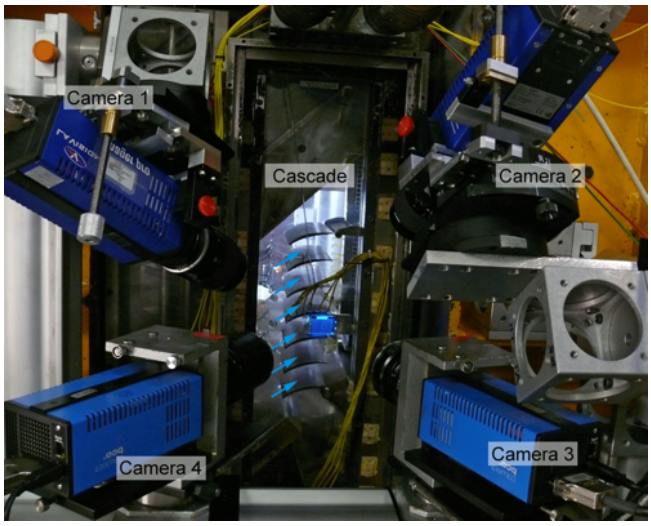

Figure 3: Tomo PIV camera setup and back-illuminated calibration target on a micro traverse

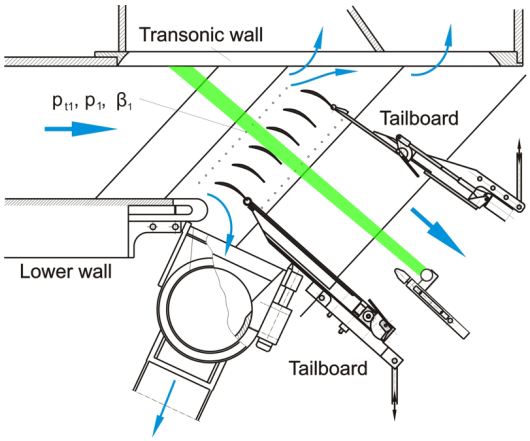

Figure 4: The TGK test section and light-sheet orientation

diameter onto inner tube diameter. Together with a cylindrical lens positioned inside of the probe the beam is enlarged in one dimension to achieve a height of the sheet of 25 mm in the FOV. The two cylindrical lenses of the second doublet focus the sheet waist at varying distances depending on the spacing between the lenses. This leads to a variable thickness of the sheet within the field of view. With the aid of spaces a reliable and quick variation of sheet thickness can be achieved even during wind tunnel operation.

In order to increase the light sheet thickness in the FOV and at the same time prevent damage to optical components in the probe, the beam waist is shifted upstream of the FOV, away from the probe itself. In conjunction with the limited aperture of 6.6×9.4 mm^2 provided by the Laval nozzle at the probe tip, the maximum achievable sheet thickness is limited to about 5 mm in the probe volume. The maximum light sheet thickness, as measured with a beam profiler, is 3.5 mm FWHM within the FOV at 450 mm distance from the probe tip (Fig. 6). The higher order transverse modes of the flash lamp pumped laser result in a more flat top profile of the thick sheet and therefore strongly deviates from the Gaussian fit. The minimum achievable light sheet thickness is 1.1 mm FWHM at the waist which is used for the stereo PIV reference measurements. The integral pulse energy is 50 mJ net within the FOV.

Cameras no.2 and no.3 observe the illuminated volume with a backward scattering angle of $-15°$ at effective f-numbers of 14 and 11, respectively, in order to keep astigmatic distortion at an acceptable level. Therefore these cameras have the lowest sensitivity in the present imaging configuration. At maximum sheet thickness these cameras deliver a minimum net signal of about 150 counts per particle (after background intensity subtraction) which corresponds to only a few percent of the camera's dynamic range (14 bit for camera models pco.1600 / pco.2000).

The cascade wind tunnel facility is seeded with an atomized paraffine-ethanol mixture (1:2) dispersed by two atomizers. An impactor and a dryer between atomizer and test section limited the maximum droplet diameter to approximately 1 μm. In an effort of improving the global seeding homogeneity a seeding injection rake was installed on the screens within the settling chamber upstream of the test section. This ensured the distribution of the particles over a larger area compared to streamline seeding. A response time evaluation of the applied seeding can be found in [4] and reports a shock response time of $0.77 \pm 0.15\,\mu$s based upon velocity profiles measured across a normal shock at $M_1 = 1.25$. The average response length corresponds to $0.23 \pm 0.045\,\mu$m. Based on Stokes drag law for spherical particles and a particle density of $\rho_p = 0.85$ g/mm^3 with the ethanol part fully evaporated and a maximum particle slip velocity of $\Delta u = 150$ m/s this would lead to an average particle diameter of about $d_p = 0.4\,\mu$m.

3.1 Camera calibration and accuracy

The volume was calibrated with a traversed micro target [5] which consists of back-illuminated calibration points at a spacing of 2 mm and a diameter of 0.4 mm. The lateral accuracy of point spacing is $\pm 0.3\,\mu$m. Seven calibration planes at 1 mm z-spacing were recorded. The vendor of the micro traverse states a positioning accuracy in z of $\pm 2\,\mu$m.

The measured point correspondences of world and camera coordinates are used to fit mapping functions according to world-to-image and image-to-world projection. The averaged residuals of the least squares optimization can be found in table 3. The residuals of the world-to-image projection range from 0.16 to 0.3 pixel depending on the mapping function and camera. The averaged residuals per calibration plane (not shown here) are consistently lower. An explanation for this effect might be a slight nonlinearity in the travel of the traverse. This is also confirmed by the fact that the residuals increase as the camera viewing angle with respect to the normal of the plate increases. The highest reprojection error arises for camera no.2 which has a 37° off-normal viewing angle.

Global image shifts due to tunnel vibrations were monitored simultaneously with tomographic measurements. The particle image recordings additionally contain images of laser illuminated small reference marks on the Perspex sidewalls. These small marks were correlated with appropriate regions of the ensemble averaged intensity image of the PIV recording. This a posteriori correction is only possible for the measurement volumes at 4 and 8 mm distance from the sidewall, where both marks and particles still are within camera focus. Fig. 7 shows the image shifts due to tunnel vibrations. The shifts are on the order of ≈ 0.5 pixel for cameras no.3 and no.4 and

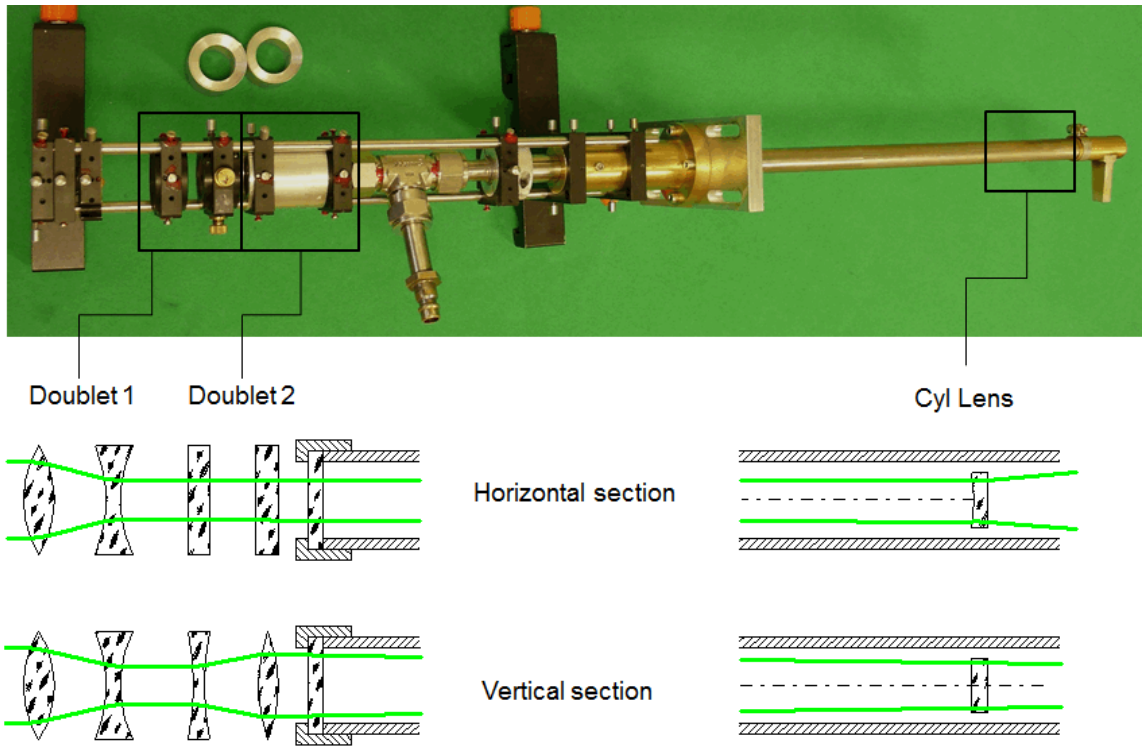

Figure 5: Optical design of the light-sheet probe

of ≈ 1 pixel for camera no.1. By comparison, the sizes of particle images vary between $2-6$ pixel depending on the camera view (see Tab. 2). An additional correction of global image shifts is subject of ongoing efforts.

3.2 Particle volume reconstruction

Three dimensional reconstruction of the imaged particle volume is achieved with the maximum entropy reconstruction technique (MENT) [6]. This algorithm was chosen because it offers a number of advantages with respect to the more established methods such as MART or MLOS-SMART [1]. Foremost MENT can significantly increase reconstruction speed [2] because the computational complexity is low and is limited to the calculation of products, sums and ratios of intensities, whereas SMART requires exponentiation and elaborate calculation of weighting factors. Bilsky et al. [2] have found MENT to converge already after 1 to 3 iterations while MLOS-SMART requires on the order of 10 to 20 iterations to achieve similar convergence levels. A further acceleration of the first step of MENT can be obtained if the processing of rows of h_j^{k+1} is parallel distributed on several cores. This was achieved using the OpenMP library [7]. The memory demand of MENT is much lower as for MART or SMART. The processing of the pseudo images h at each time step is based on $2 \times nx_j \times ny_j$ arrays with nx and ny being the width and height of each view j. Conventional MART or SMART algorithms need images and all 3-D intensities above zero possibly plus weights to be stored in RAM during processing. MENT recovers the volume intensities only in the second step. Thus the processed volume slices can directly be transferred to the hard disc. A speed up of volume processing can be achieved by distributed processing of volume slices on several cores. To give an example, 20 iterations of a MLOS-SMART reconstruction of two time steps of a volume of 0.5 GVoxel based on four views of approx. 2 MPixel

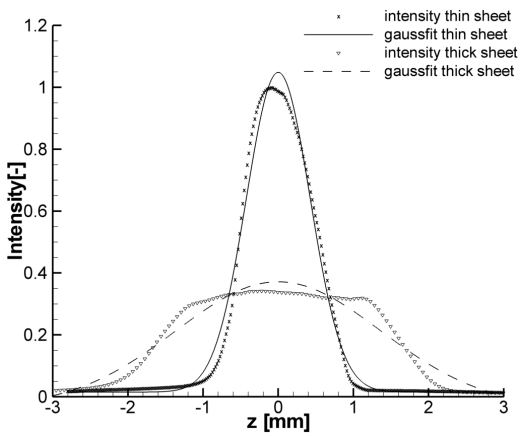

Figure 6: Light sheet intensity profile vs. volume depth of thick and thin sheet

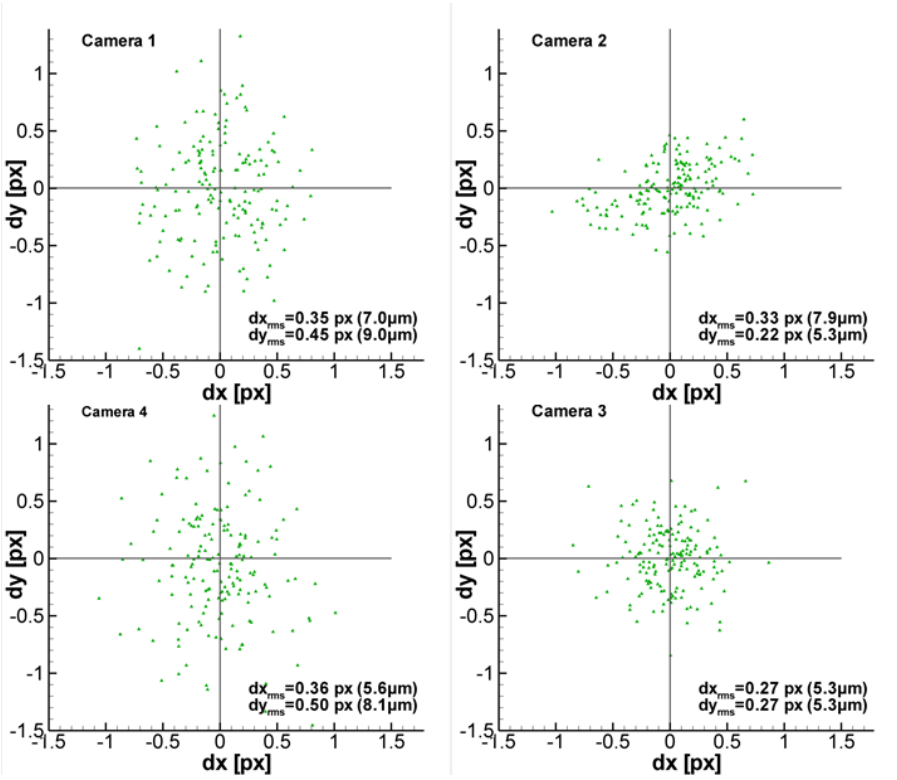

Figure 7: Global image shifts due to tunnel vibrations. Numbers in brackets show approximately the corresponding shifts in object space

Table 3: Residuals of world-to-image mapping (fwd.) in $[pixel]$ and image-to-world mapping (bwd.) in $[\mu m]$ after least squares minimization of the reprojection error

Mapping algorithm	Camera 1		Camera 2		Camera 3		Camera 4	
	fwd. $[pixel]$	bwd. $[\mu m]$	fwd. $[pixel]$	bwd. $[\mu m]$	fwd. $[pixel]$	bwd. $[\mu m]$	fwd. $[pixel]$	bwd. $[\mu m]$
Pinhole w/o. distorsions	0.30	-	0.33	-	0.24	-	0.27	-
Ratio of 2nd order poly.	0.22	4.7	0.24	6.6	0.17	3.4	0.24	3.9
3rd order poly.	0.22	4.6	0.24	5.9	0.16	3.1	0.23	3.9

can take in the order of 20 minutes on a 12-core Intel workstation at 2.66 Ghz and 24 GB RAM. The processing of two time-steps of the same volume of MENT took in the order of 3 min on the same workstation.

The MENT algorithm reconstructs the three-dimensional intensity distribution in two steps. The first step (cf. Fig. 8, left) calculates the two-dimensional discrete functions or so-called pseudo images h_j for each view based on the multiple view images p_j [2]. Following [6] the pseudo images h_j are first initialized using:

$$\begin{aligned} h_j^0(x_I, y_I) &= 1 \quad \text{if } p_j(x_I, y_I) > 0 \\ h_j^0(x_I, y_I) &= 0 \quad \text{if } p_j(x_I, y_I) = 0 \end{aligned} \tag{1}$$

Subsequently, in order to calculate 2, the pixel coordinates x_I, y_I of view j are projected into the volume, giving the coordinates of the line-of-sight L as a function of x_I, y_I, z. The coordinates of all members l of the lines-of-sight $L(z)$ are than projected onto each image $j \neq i$ in order to obtain coordinates of the epipolar lines of x_I, y_I. The intensities h_{il}^k along the epipolar line are found by image interpolation. Here, bilinear interpolation of the 4-neighborhood in h_i^k is used. In order not to undersample epipolar intensities, the increment Δz_1 in step one was chosen to be $0.5\Delta z_2$ with Δz_2 being the voxel depth at the final reconstruction. The denominator in 2 is given by the product of h_{il}^k of each view $j \neq i$ summated along L. Finally, the new value of h_j^{k+1} is calculated by the ratio of the measured intensity p_j divided by the sum of intensity products along the epipolar lines:

$$h_j^{k+1} = \frac{p_j}{\frac{1}{V} \sum_{l \in L} \prod_{i \neq j} h_{il}^k} \tag{2}$$

The aim of this optimization is that the measured intensity at $p_j(x_I, y_I)$ equals the summation of intensities along the line of sight in the reconstructed volume. This state is expected if 2 converges to 3. Here the measured intensity at $p_j(x_I, y_I)$ equals the line-of-sight sum

along L of the products of intensities of h at the corresponding epipolar lines plus a residuum ε.

$$p_j = \left(h_j \frac{1}{V} \sum_{l \in L} \prod_{i \neq j} h_{il} \right) + \varepsilon \tag{3}$$

Finally, the volume recovery is performed after convergence of pseudo image intensities. The 3-D intensities at each voxel position x, y, z are found by multiplication of the intensities of the pseudo-images at the projected coordinates x_I, y_I (see Fig. 8,right and 4). The intensities of h_j at x_I, y_I are interpolated bilinearly from the 2×2-neighborhood. The intensity product is finally scaled to lie in a 16bit unsigned integer range.

$$I(x,y,z) = \frac{1}{V} \prod h_j(x_I, y_I) \tag{4}$$

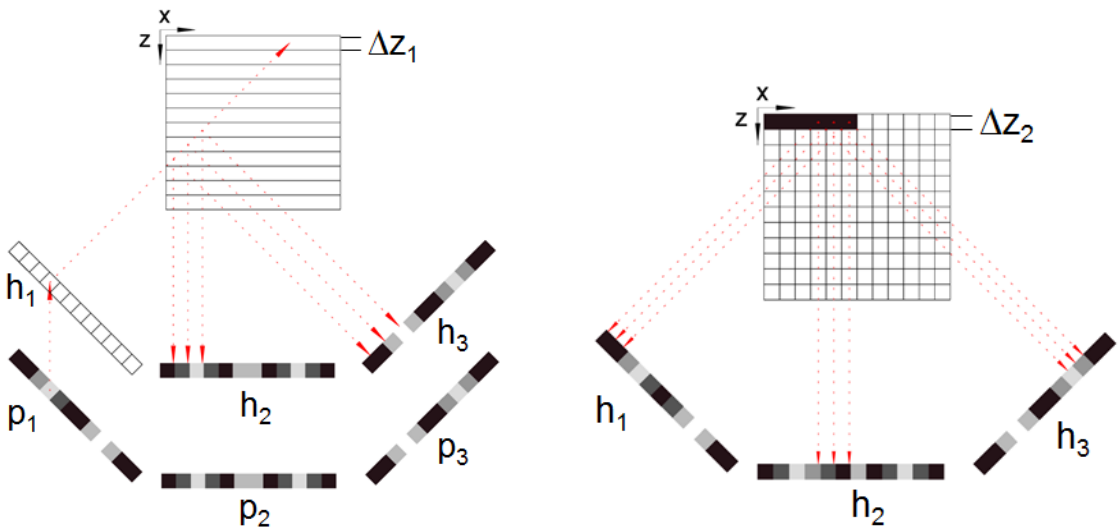

Figure 8: Reconstruction of the 3-D particle distribution using MENT: generation of pseudo images (left), volume recovery (right)

3.3 Particle displacement recovery

State-of-the-art cross-correlation processing is used for particle displacement recovery in both planar and volume PIV. Both algorithms employ a resolution pyramid the starts at a rather coarse grid and stepwise increases resolution while continually updating a predictor field [9, 8]. To increase processing speed, factor N image or volume downsampling is applied by summing N^2 adjacent pixels or N^3 voxels, respectively. At a given resolution level integer-based sample offsetting is applied in a symmetric fashion using the estimate from the previous resolution step [12, 11]. Intermediate validation is based on normalized median filtering as proposed by Westerweel & Scarano [13]. Once the desired final spatial resolution is reached image or volume deformation based on third-order B-splines [10] is applied at least twice to further improve the match between the image or volumes and thereby improving the displacement estimates. The processing codes are highly parallelized using OpenMP [7] to achieve optimal data throughput.

An overview of the involved processing steps is given in table 4 and illustrates that optimal data recovery can only be achieved through careful adjustment of these parameters. Both conventional (stereo) PIV and tomographic PIV are very susceptible to laser flare, such as light reflected by the blades or scattered by slight scratches or seeding deposits on the windows. Therefore image data is first processed using background subtraction and spatial filtering to enhance overall contrast thereby improving the visibility of particle images.

4. Results

4.1 Stereo PIV measurements

Stereo PIV measurement data is acquired from a thin light sheet setup using cameras no.1 and no.3 at combined viewing angle of 50°. The image data was processed with PIVview 3.5 (PIVTEC GmbH, Germany) using the PIV processing parameters summarized in table 4. Fig. 9 shows the secondary flow velocities obtained by averaging $N = 510$ individual PIV recordings. In order to emphasize the chordwise vortex evolvement, six orthogonal planes are extracted from nine stereo PIV planes. The color represents the v-w magnitude while the vectors show the in plane v-w velocity. Secondary flow velocities in-between the SPIV planes are obtained by inverse distance interpolation. Due to interaction with the main flow the vortex is deformed and velocities in the vicinity of the end wall are clearly increased. The separation region on the blades suction side (see Fig. 1) causes an increase of secondary flow velocities near the blades suction side.

4.2 Tomographic PIV measurements

Fig. 10 shows time-averaged velocities at two neighboring thick sheet positions and boundaries of each reconstructed domain. Six secondary flow planes within the volume are plotted to show the vortex evolvement. The colored contour represents v-w-magnitude,

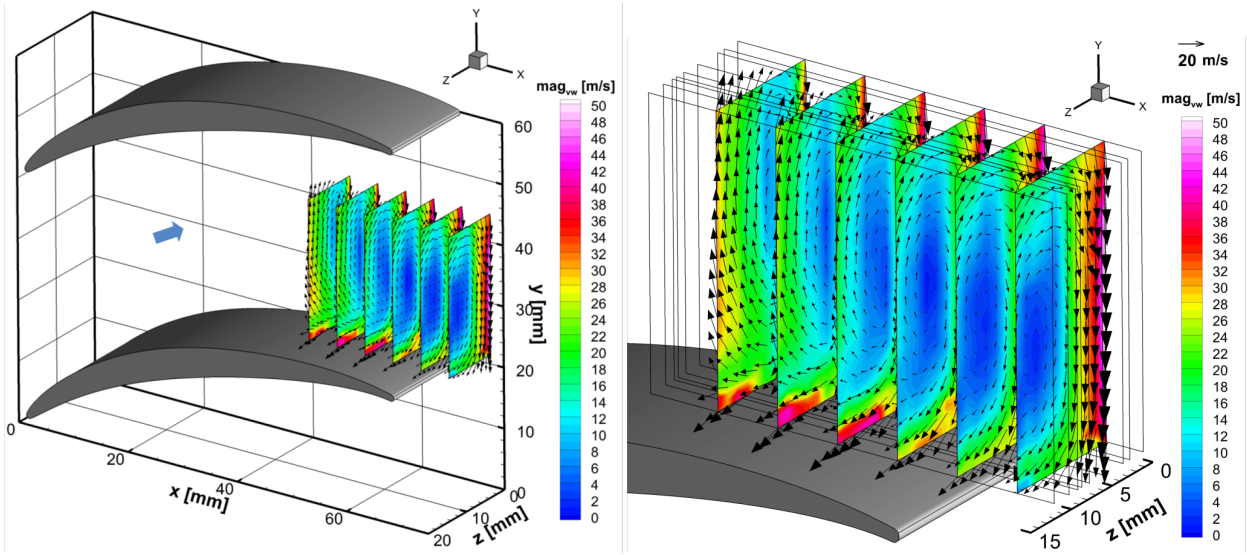

Figure 9: Time averaged secondary flow velocities obtained from averaged SPIV measurements at 9 planes each with 1mm sheet thickness; overview (left) and detailed flow field and boundaries of the SPIV planes (right)

that is, the in-plane velocity. Regions outside the common intersection of all cameras are blanked as well as regions which have light sheet intensity clearly below 50%. Within each plane only the in-plane components of every third vector are plotted to enhance the visibility of the secondary flow which otherwise would be lost in the presence of the strong out-of-plane component (mean flow). The passage vortex can clearly be identified. The v-w magnitudes are comparable to stereo PIV results (see Fig. 9, right). The increased secondary flow velocities near the blades suction side can also be observed in stereo PIV results. The magnitudes in this region are lower due to strong background intensity near the blade surface observed by obliquely viewing cameras no.1 and no.2.

Table 4: Evaluation parameters of stereo PIV and tomographic PIV

	Stereo PIV (thin sheet)	Tomographic PIV (thick sheet)
field of view (FOV)	$\approx .36 \times 24$ mm^2	$\approx .36 \times 24$ mm^2
light sheet thickness (FWHM)	1.1 mm	3.5 mm
size of ROI, magnification	1800×1200 pixel at 50 pixel/mm	$1800 \times 1200 \times 300$ voxel at 50 voxel/mm
image enhancement	Subtraction of min. image 3x3 median filter 7x7 high pass filter 3x3 low-pass filter	Subtraction of min. image local minimum subtraction (5x5 kernel) normalization by avg. image intensity clipping
mapping algorithm	2nd order projection map and disparity correction	ratios of 2nd order polynomials
image interpolation	4th order B-Spline	bi-linear
reconstruction algorithm	-	MENT, 2 iterations
interrogation method	multi-resolution (3 levels) image deformation (3 passes)	3-D correlation, multi-resolution (3 levels) volume deformation (3 passes)
sub-pixel peak location	Whittaker reconstruction	3-point Gauss fit
interrogation window	64×48 pixel	$64 \times 32 \times 32$ voxel
sampling grid	32×24 pixel	$32 \times 16 \times 16$ voxel
validation	maximum displacement difference < 5 pixel normalized median filter (≤ 3)	normalized median filter (≤ 3) light sheet intensity $> 50\%$
final data grid	59×49 vectors	$54 \times 74 \times 13$ vectors

5. Discussion and Conclusion

The investigation presented herein demonstrates the applicability of volumetric PIV in a highly loaded compressor cascade at $M_1 = 0.60$. With four simultaneous camera views it possible to measure the complex corner flow of the cascade volume at three regions with respect to the side wall. The final vector resolution is $54 \times 74 \times 13$ vectors at a spacing of 0.64 mm in x (chord-wise direction) and a spacing of 0.32 mm in y and z. Averaged results of the corner flow are presented to show conformance to the expected flow. The measurements were complemented with stereo PIV (SPIV) measurements at distinct planes to provide a basis for comparison between the employed volumetric techniques.

Application of tomographic and other multi-view imaging techniques on facilities with limited optical access presents a number of challenges some of which are difficult if not impossible to solve. Geometric constraints imposed by windows limit not only the

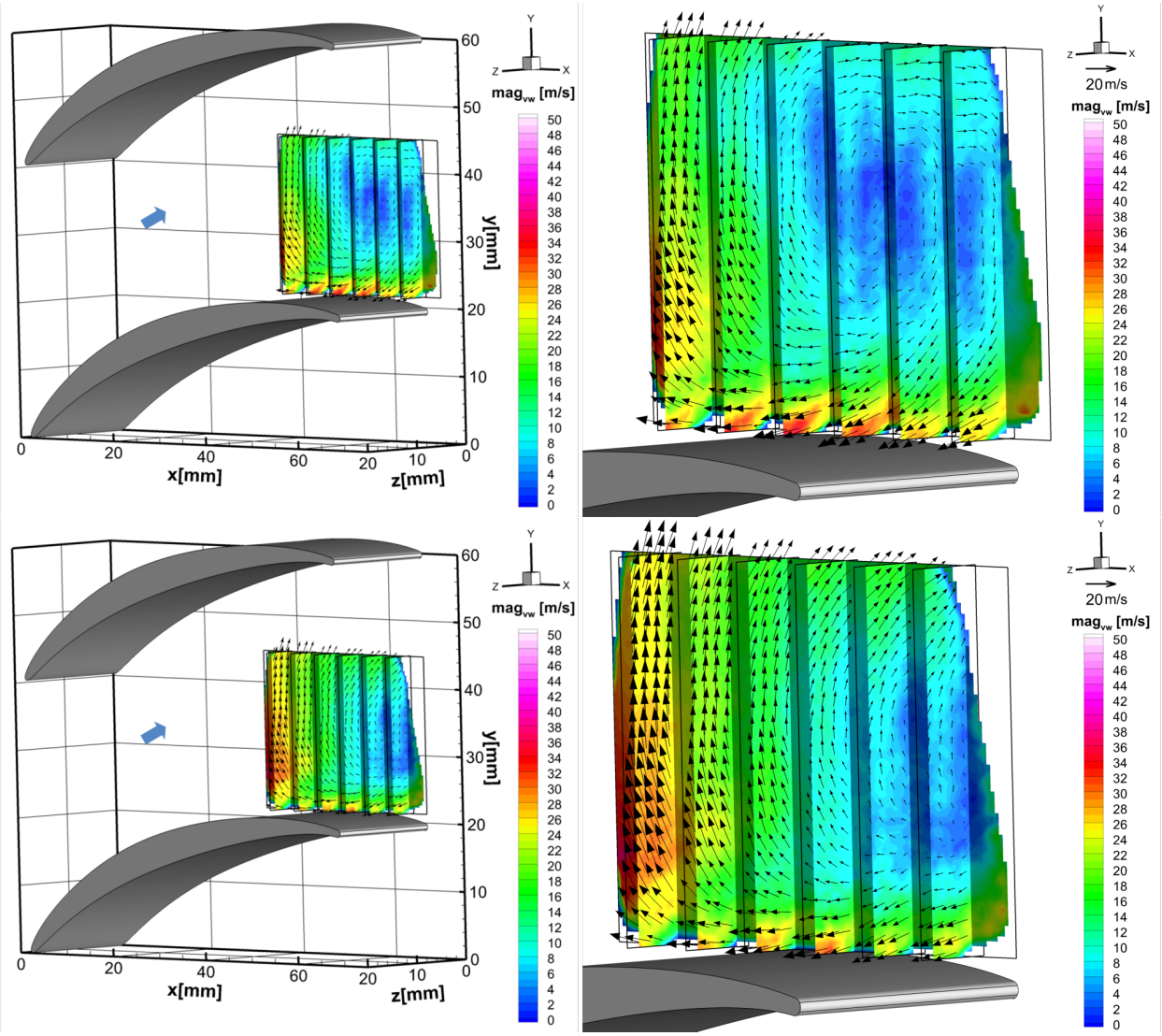

Figure 10: Average of $N = 100$ tomographic measurements for a volume of $36 \times 24 \times 4$ mm^3 at $z = 8$ mm distance from the end wall (top), $z = 11$ mm (bottom); overview (left) and detailed flow field with boundaries of reconstructed domain (right). Every third vector along each dimension is plotted

maximum possible viewing angles but more importantly frequently constrain the commonly viewed domain (volume of interest), in particular if this domain is located further inside the facility. Laser flare due to light scattering within the facility can pose significant problems since it affects each camera view differently. In the present case the camera views aligned with the span of the airfoil was only weakly affected by the laser light scattering off the airfoil, whereas the inclined camera views were strongly affected by light scattering off the airfoil which caused a loss of signal in these areas. Similarly measurements in close proximity to the perspex endwall are hampered by light scattered by surface scratches and seeding residue.

Given these challenges the choice of applying tomographic/photogrammetric methods to turbomachinery facilities has to be carefully assessed in the context of the physics to be investigated. Foremost, the application of these methods only is justified if the flow itself is highly unsteady and cannot be adequately mapped using planar techniques, whose implementation generally is significantly less complex. Another aspect to be considered is that for tomographic/photogrammatic methods the gain of information in depth comes at the price of reduced in-plane resolution - unless sensor resolution is increased proportionally. Therefore the range of resolvable flow features is considerably reduced in comparison to planar methods. On the other hand the access to three-dimensional, three-component unsteady velocity data alongside with the fully resolved three-dimensional strain tensor makes tomographic/photogrammetric velocimetry very attractive to reliably capture the flow physics and to provide important validation data.

Acknowledgments

Funding is provided in part by the EU-project AFDAR (Advanced Flow Diagnostics for Aeronautical Research, project no. 265695) of the 7th Framework Program whose support is gratefully acknowledged. We are deeply indebted to our colleagues Andreas Hergt and Sebastian Grund for their patience and support in operating the transonic cascade facility and like to thank Melanie Voges for the support during the PIV campaign.

REFERENCES

[1] Atkinson, C., Soria, J.: An efficient simultaneous reconstruction technique for tomographic particle image velocimetry. Experiments in Fluids **47**, 553–568 (2009)

[2] Bilsky, A.V., Markovich, D.M., Tokarev, M.P., Lozhkin, V.A.: Low computation cost reconstruction technique for tomo-piv. In: 16th Int Symp on Applications of Laser Techniques to Fluid Mechanics (2012)

[3] Hergt, A., Steinert, W., Grund, S.: Design and experimental investigation of a compressor cascade for low reynolds number conditions. In: 21th International Symposium on Air Breathing Engines, Busan (South Korea), ISABE-2013-1104 (2013)

[4] Klinner, J., Hergt, A., Beversdorff, M., Willert, C.: Visualization and piv measurements of the transonic flow around the leading edge of an eroded fan airfoil. In: 16th Int Symp on Applications of Laser Techniques to Fluid Mechanics (2012)

[5] Klinner, J., Willert, C.: Tomographic shadowgraphy for three-dimensional reconstruction of instantaneous spray distributions. Experiments in Fluids **53**, 531–543 (2012). DOI 10.1007/s00348-012-1308-2. URL http://dx.doi.org/10.1007/s00348-012-1308-2

[6] Minerbo, G.: Ment: A maximum entropy algorithm for reconstructing a source from projection data. Graphics and Image Processing (10) (1979)

[7] OpenMP Architecture Review Board: OpenMP application program interface version 3.1 (2011). URL http://www.openmp.org/mp-documents/OpenMP3.1.pdf

[8] Raffel, M., Willert, C., Wereley, S., Kompenhans, J.: Particle Image Velocimetry, A Practical Guide. Springer Berlin-Heidelberg (2007)

[9] Scarano, F.: Iterative image deformation methods in piv. Measurement Science and Technology **13**(1), R1 (2002). URL http://stacks.iop.org/0957-0233/13/i=1/a=201

[10] Thévenaz, P., Blu, T., Unser, M.: Interpolation revisited. IEEE Transactions on Medical Imaging **19**(7), 739–758 (2000)

[11] Wereley, S.T., Meinhart, C.D.: Second-order accurate particle image velocimetry. Experiments in Fluids **31**(3), 258–268 (2001). DOI 10.1007/s003480100281. URL http://dx.doi.org/10.1007/s003480100281

[12] Westerweel, J., Dabiri, D., Gharib, M.: The effect of a discrete window offset on the accuracy of cross-correlation analysis of digital piv recordings. Experiments in Fluids **23**(1), 20–28 (1997). DOI 10.1007/s003480050082. URL http://dx.doi.org/10.1007/s003480050082

[13] Westerweel, J., Scarano, F.: Universal outlier detection for piv data. Experiments in Fluids **39**(6), 1096–1100 (2005). DOI 10.1007/s00348-005-0016-6. URL http://dx.doi.org/10.1007/s00348-005-0016-6